PHYSICAL REVIEW MATERIALS **1**, 053604 (2017)

Neural network potential for Al-Mg-Si alloys

Ryo Kobayashi,[1,2,*] Daniele Giofré,[3] Till Junge,[4] Michele Ceriotti,[3] and William A. Curtin[4]
[1]*Department of Scientific and Engineering Simulation, Nagoya Institute of Technology, Gokiso-cho, Showa-ku, Nagoya 466-8555, Japan*
[2]*Center for Materials research by Information Integration (CMI2), Research and Services Division of Materials Data and Integrated System (MaDIS), National Institute for Materials Science (NIMS), 1-2-1 Sengen, Tsukuba, Ibaraki 305-0047, Japan*
[3]*Institute of Materials Science, École Polytechnique Fédérale de Lausanne, CH-1015, Vaud, Switzerland*
[4]*Institute of Mechanical Engineering, École Polytechnique Fédérale de Lausanne, CH-1015, Vaud, Switzerland*

(Received 4 August 2017; published 30 October 2017)

The 6000 series Al alloys, which include a few percent of Mg and Si, are important in automotive and aviation industries because of their low weight, as compared to steels, and the fact their strength can be greatly improved through engineered precipitation. To enable atomistic-level simulations of both the processing and performance of this important alloy system, a neural network (NN) potential for the ternary Al-Mg-Si has been created. Training of the NN uses an extensive database of properties computed using first-principles density functional theory, including complex precipitate phases in this alloy. The NN potential accurately reproduces most of the pure Al properties relevant to the mechanical behavior as well as heat of solution, solute-solute, and solute-vacancy interaction energies, and formation energies of small solute clusters and precipitates that are required for modeling the early stage of precipitation and mechanical strengthening. This success not only enables future detailed studies of Al-Mg-Si but also highlights the ability of NN methods to generate useful potentials in complex alloy systems.

DOI: 10.1103/PhysRevMaterials.1.053604

I. INTRODUCTION

Lightweight alloys that show significant solid solution strengthening and precipitation strengthening have been developed for decades and are widely used in automotive and aviation industries. The 6000 series Al-Mg-Si alloys are an important class of lightweight alloys that can be formed both by casting and wrought processes. The processes of clustering of solute atoms and forming of Guinier-Preston (GP) zones or precipitates significantly affect the strength of the alloy as a function of aging time and temperature. The strength is determined by the interaction of dislocations with the evolving microstructure (random solutes, solute clusters, GP zones, and precipitates). As a result, considerable experimental effort has been made to control the formation of precipitates by means of heat treatment and/or control of the alloy composition. However, direct observation of small clusters and precipitates is challenging, making it difficult to understand the growth mechanisms, and associated strengthening mechanisms, from early stages of precipitation up to the peak aging at which the maximum strength is reached.

Atomistic simulations such as *ab initio* calculation, molecular dynamics (MD), and kinetic Monte Carlo (KMC) are powerful tools for studying the early stage of clustering of solutes and interaction between dislocations and solutes, clusters, and precipitates. *Ab initio* methods provide chemical accuracy for arbitrary atomic arrangements but are computationally prohibitive, with respect to both sizes and times, for addressing problems related to clustering, precipitation, and strength. Thus MD and KMC methods must be used, but these methods require the existence of interatomic potentials for all the interactions among alloying elements, and require accurate potentials for realistic predictions. The development of accurate multicomponent interatomic potentials has proven to be a serious challenge, and thus a significant impediment to the application of MD and KMC methods to alloys.

In spite of the challenges, many efforts to create interatomic potentials have been made. For single-element metals and solid solution alloys, the embedded atom method (EAM) potentials [1] have been widely used because of their reasonable accuracy and simple form. The modified EAM (MEAM) [2] approach enables additional directional bonding and so has been pursued for binary alloys that form intermetallic compounds [3,4]. However, it is difficult for both EAM and MEAM methods to reproduce a wide variety of compound phases for alloys with more than two components. For instance, Jelinek *et al.* developed an MEAM potential with pair and triplet interaction parameters for the five elements Al, Mg, Si, Cu, and Fe that reproduces several properties of binary compounds. However, generally, these potentials do not provide "chemical accuracy" at the level needed ($\sim k_\mathrm{B}T$) for realistic simulations at characteristic temperatures ($T \sim 300$–600 K). For the particular Al-Mg-Si ternary system, the lattice constants and heats of formation of important precipitate phases are not well-predicted. Thus there continues to be a great need for accurate multicomponent interatomic potentials.

In this paper, we develop a neural-network (NN) interatomic potential for the ternary Al-Mg-Si system that is useful for the study of precipitation processes and strengthening of the Al 6xxx alloys. The NN potential approach, developed by Behler and Parrinello [5], is one of several classes of machine-learning potentials, such as the Gaussian approximation potential (GAP) [6,7] and the linear regression potential [8]. These potentials introduce a large number of functions and parameters with no direct physical interpretation, rather than a few functions based on physical concepts, but the high flexibility then allows for the fitting of complex potential energy landscapes that govern the observed structures and the evolution of a material system. Previous studies show

---

[*] kobayashi.ryo@nitech.ac.jp

that the NN potential can reproduce the complex potential energy landscape of binary systems such as TiO_2 [10] and phase-change materials [11], and ternary systems such as Cu clusters on ZnO surface [9].

Recently, Hajinazar *et al.* [12] developed an approach to construct an NN potential for the ternary alloy Cu-Pd-Ag, in which the NN potential was optimized hierarchically from unary to ternary systems. Although this approach has some practical advantages, some important properties for precipitation processes such as the heats of solution (e.g., Pd in fcc Cu) are not in good agreement with reference values, up to ∼0.2 eV. Here, we demonstrate the application of the NN approach for the development of potentials for the Al-Mg-Si ternary system, as optimized to match an extensive set of reference data obtained by *ab initio* calculations. We thus show that the NN approach has promise as an approach for obtaining interatomic potentials for complex alloys and we provide a specific potential for the study of the technologically valuable Al 6xxx alloy system.

The remainder of this paper is organized as follows. The simulation methods and geometries of calculated structures are described in Sec. II. The details of the NN potential and the procedures for parametrization are reviewed in Sec. III. The properties of pure Al as predicted by the NN potential are presented in Sec. IV and the properties of the ternary system are presented in Sec. V. We summarize our work in Sec. VI.

II. SIMULATION METHODS AND GEOMETRIES

The energies and forces of all the structures used for training the network are calculated by density functional theory (DFT) using QUANTUM ESPRESSO [13]. In the DFT calculations, the generalized gradient approximation (GGA) parameterized by Perdew *et al.* [14] (PBE) is used for the exchange-correlation functional, and ultrasoft pseudopotentials [15,16] are employed with ten, three, and four valence electrons for Mg, Al, and Si, respectively. The wave functions are expanded using plane waves with the cutoff energy 35 Ry (476 eV) and integration over the irreducible Brillouin zone is done using the Monkhorst-Pack method with a k-point pitch less than $0.1\ \text{Å}^{-1}$ and an electron occupation over bands is smeared by a Gaussian function with width 0.05 Ry. These values were validated via a study of convergence of the lattice constant and bulk modulus. To estimate the uncertainty within the DFT scheme, some computations were repeated using the so-called PBEsol exchange-correlation functional [17].

Calculations using the NN potential and optimization of parameters in the NN potential are performed using our own MD program, NAP [18]. Calculations using the MEAM potentials of both Jelinek's and Kim's [20] are performed using the large-scale atomic/molecular massively parallel simulator (LAMMPS) [21].

In calculations of pure bulk structures and ordered compounds, the minimum conventional cells are used with periodic boundary conditions (PBCs) in all the directions. In finite temperature calculations of pure Al to compute the thermal expansion coefficient, we use $3 \times 3 \times 3$ cubic FCC cells and equilibrate the system to the target temperature using the Langevin thermostat [22] and the target pressure (0 GPa) using the Berendsen barostat [23] over a total time of 10 ps. The atomic volume at a given temperature is obtained as the average volume during 10 ps after the initial 10-ps equilibration time.

In calculations of single solutes/vacancies and solute-solute or solute-vacancy interactions, we use $4 \times 4 \times 4$ cubic FCC cells with one or two Al atoms replaced by solutes as appropriate. In calculations of "random" distribution of solutes, $2 \times 2 \times 2$ cubic FCC cells are used and a half of the atoms (16) are chosen randomly and replaced with two vacancies and 14 solute atoms, Mg and Si. In both cases, PBCs are applied to all the directions and atom positions are relaxed with the lattice constants being fixed to that of pure Al. These are reference calculations of specified structures for input into the NN algorithm, and so there is no need to relax these structures fully.

In calculations of stacking faults, the simulation cell is oriented with axes along $[1\bar{1}0]$, $[11\bar{2}]$, and $[111]$ as x, y, and z directions, respectively. PBCs are used along x and y and the surfaces along z are free with a vacuum region wider than 11 Å. There are 12 atomic layers along z and the stacking fault is introduced by the rigid shift of upper half atoms in z followed by relaxation of all atoms only along the z direction.

In calculations of the properties for the (111), (001), and (110) surfaces, the energy versus separation is calculated by rigidly separating the upper and lower halves of atoms. The slab was made thicker than 8 Å to reduce spurious interactions between surfaces. The cell size in the plane of the surface is fixed to the bulk equilibrium value.

In calculations of precipitates, the geometry of the system follows that employed by Ninive *et al.* [24] (also shown in Fig. 7). A needle-shape precipitate is embedded into an Al matrix so that the longitudinal axis of the needle matches the [001] direction of the Al matrix. The system size normal to the longitudinal axis is proportional to the number of formula units of the precipitate embedded in the system. For example, cell sizes of 5×5, 7×7, and 12×12 are used for precipitates containing 1, 4, and 16 formula units, respectively. The lattice constant of the system is fixed to that of pure Al at equilibrium.

In calculations of dislocation-solute interactions, the system is prepared by the following steps. Firstly, we create an orthogonal FCC lattice with x, y, and z axes along $[1\bar{1}0]$, $[11\bar{2}]$, and $[111]$, with lengths 285.7, 14.8, and 219.6 Å, respectively. A vacuum region along the z axis wider than the cutoff distance of the NN potential is introduced by removing atoms. Secondly, a perfect dislocation is introduced along y at the center of x and z coordinate system by removing one atomic layer normal to x from the bottom half of the system. Relaxing the atoms while holding the z motions of atoms on (111) surfaces fixed, we obtain two partial dislocations and a stacking fault between them. The Nye tensor distribution around the dislocation cores is calculated using the method proposed by Hartley and Mishin [25]. To obtain the interaction energy between a solute and a dislocation core, one Al atom around the dislocation core is replaced with the desired solute. If the system is relaxed with no constraints, it is frequently the case that the dislocation will glide so that the solute position, relative to the dislocation, is in a low-energy position (typically, either near a partial core or far away from the dislocation). When this occurs, the measurement of "solute/dislocation interaction energy" for the original solute position is not obtainable. To overcome this problem, we fix one plane of atoms in a plane perpendicular to the dislocation line, thereby pinning the dislocation core structure in this plane. The solute is then inserted at the desired y-z position in a plane furthest from the constrained plane of atoms, the system is relaxed, and the energy is measured. Due to the constraint, the dislocation does not bow-out toward or away from the solute.

III. NEURAL-NETWORK POTENTIAL

A. Structure of the NN potential

The NN potential developed in this paper is basically the same as the one originally developed by Behler and Parrinello [5]. However, since there are some differences in detail, we describe the structure of the NN potential here.

The energy of an atom i in a structure s is defined as

$$E_i^s = \sum_m w_{1m}^2 y_{i,m}^1, \tag{1}$$

$$y_{i,m}^1 = f_\mathrm{a}\left(\sum_n w_{mn}^1 G_{i,n}\right). \tag{2}$$

Here, w_{mn}^l is the weight of a line from a node n in the $(l-1)$th layer to a node m in lth layer of the NN, and $y_{i,m}^l$ is the value of node m in lth layer, Also, $G_{i,n}$, the so-called *symmetry function*, is the nth input, which depends on the interatomic bond distances R_{ij} from an atom i to a surrounding atom j. The activation function $f_\mathrm{a}(x)$ is defined using the sigmoid function as

$$f_\mathrm{a}(x) = \frac{1}{1+\mathrm{e}^{-x}} - \frac{1}{2}, \tag{3}$$

where $1/2$ is subtracted from the sigmoid function so that $y_{i,m}^1$ becomes zero when all the inputs are zero, resulting in the energy being zero.

There are many choices of the symmetry functions. Here, we employ the Gaussian function

$$G_{i,n} = \sum_{j\neq i} \mathrm{e}^{-\eta_n (R_{ij}-R_n)^2} f_\mathrm{c}(R_{ij}), \tag{4}$$

where η_n and R_n are the parameters that are determined heuristically before training the network. The cutoff function $f_\mathrm{c}(R)$ is defined as

$$f_\mathrm{c}(R) = \begin{cases} 1, & \text{for } R \leqslant R^*, \\ \frac{1}{2}\left[\cos\frac{\pi(R-R^*)}{(R_\mathrm{c}-R^*)}+1\right], & \text{for } R^* < R \leqslant R_\mathrm{c}, \\ 0, & \text{for } R > R_\mathrm{c}. \end{cases} \tag{5}$$

where R_c is the cutoff radius and $R^* = 0.9R_\mathrm{c}$.

B. Training of the network

The objective function to be minimized in training of the NN potential is

$$\mathcal{L}(\{w\}) = \frac{1}{2M}\sum_s^M \left[\left(\frac{\Delta E^s}{\varepsilon_\mathrm{e}^s}\right)^2 + \sum_i^{N_\mathrm{a}^s}\sum_\alpha^{xyz}\frac{1}{3N_\mathrm{a}^s}\left(\frac{\Delta F_{i,\alpha}^s}{\varepsilon_\mathrm{f}^s}\right)^2\right], \tag{6}$$

where $\Delta E^s = (E^{s,\mathrm{NN}} - E^{s,\mathrm{ref}})/N_\mathrm{a}^s$ and $\Delta F_{i,\alpha}^s = F_{i,\alpha}^{s,\mathrm{NN}} - F_{i,\alpha}^{s,\mathrm{ref}}$ are the differences in energies and force components, respectively, as obtained by the NN potential and the DFT calculations. The superscript s indicates the index of a sample, N_a^s is the number of atoms in the sample s, and M is the number of samples. The quantities ε_e^s and ε_f^s are the convergence criteria for the energy per atom and the force component for a sample s, respectively; the objective function $\mathcal{L}$ becomes less than one when ΔE^s and $\Delta F_{i,\alpha}^s$ are smaller, on average, than these convergence values.

A parameter-rich model like the NN can often show overfitting, in which the model is well optimized to the training set data but reproduces very poorly data not included in the training set. This is also known as low transferability of the interatomic potential. There are various ways to avoid the overfitting, such as the *early stopping* approach [10,26], which stops the optimization before the overfitting begins, and the *weight decay* approach [26], which adds a penalty term to $\mathcal{L}$ to suppress the parameters having large values, which usually causes the overfitting. Because it is not easy to determine when to stop the optimization in the *early stopping*, we adopted the *weight decay* approach by adding a penalty term, the so-called *ridge penalty*, to Eq. (6) as

$$\mathcal{L}^*(\{w\}) = \mathcal{L}(\{w\}) + \lambda\sum_i w_i^2, \tag{7}$$

where λ is the penalty parameter to improve the generalization or transferability of the NN potential. The hyperparameter λ is determined heuristically to be as large as possible so that the penalty term is small enough not to exceed the $\mathcal{L}$ value. The minimization of the function $\mathcal{L}^*(\{w\})$ is carried out using a quasi-Newton method, the Broyden-Fletcher-Goldfarb-Shanno (BFGS) algorithm [27].

C. Reference data

The sample configurations used to train the network should contain structures that well represent the environments that are relevant for the phenomena of interest. To create the potential used for the study of precipitation strengthening of Al-Mg-Si alloys, we used the following base structures: (i) FCC, BCC, and HCP structures of Al and Mg, diamond structure of Si; (ii) the generalized stacking fault (GSF) structure along the {111} plane of Al; (iii) several surfaces of FCC Al; (iv) FCC Al structures containing one, two, and more vacancies or solute atoms; and (v) binary compound phases among Al, Mg, and Si. From each of those base structures, we created deformed structures by changing the cell vectors of the system and displaced structures by random displacements of atoms or from MD snapshots. These displaced structures are necessary additions to the equilibrium structures because otherwise the NN could give unphysical lower energies for deformed structures relative to the true low-energy structures. In total, we generated 10 237 structures and divided them randomly into a training set used for the training and a test set used for monitoring the convergence.

D. Hyperparameters

Parameters that are not trained from data, the so-called hyperparameters must be specified before optimization. In this NN model, the hyperparameters are the number of hidden layers, the number of nodes in a hidden layer, the number of

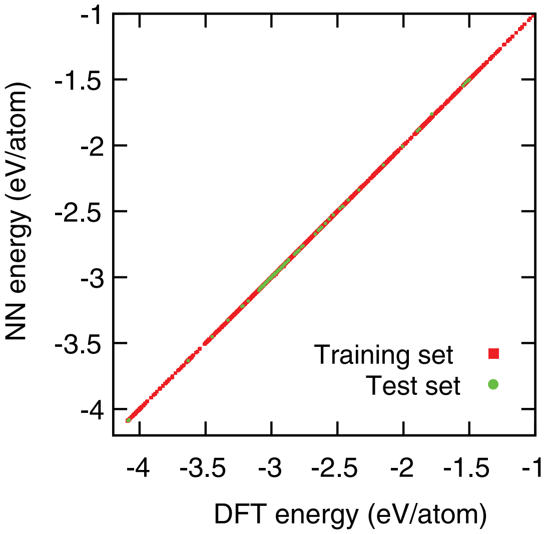

FIG. 1. Energies per atom of sample structures obtained by the NN potential and the DFT calculation. The $y = x$ line indicates ideal matching between NN and DFT values.

symmetry functions, η_n and R_n, in the Gaussian function, and the cutoff radius R_c. We determined these hyperparameters by trial and error, validating the obtained NN potential using several physical values as shown in the following sections. The resulting hyperparameters of the NN potential proposed were eventually chosen as follows: the number of hidden layers is 1 and the number of nodes in a hidden layer is 30. The number of symmetry functions for each pair is 20, so the total number of symmetry function is 120 because there are six pairs among three elements. For all the symmetry functions, $\eta_n = 10.0\ \text{Å}^{-1}$. There are 20 R_n for each pair at regular intervals from 1.5 to 5.7 Å. We set the cutoff radius $R_c = 5.8$ Å to cover third-neighbor interactions, which is important to distinguish FCC and HCP structures and to reproduce the generalized stacking fault (GSF) energy curve.

E. Optimized NN potential

Figure 1 compares the energies of sample structures predicted by the optimized NN potential against the reference values DFT. The root mean square error (RMSE) for the training data is 0.5 meV/atom. More importantly, the RMSE for the test data is 2.0 meV/atom. This indicates that the present NN potential is able to accurately reproduce all the structures in the entire sample data set, which is designed to include many structures and configurations that are relevant for modeling of evolution and mechanical performance in the Al-Mg-Si system. Because the present NN potential has 120 symmetry functions, 3600 first-layer weights and 30 second-layer weights per atom, the speed of calculating forces of the NN potential implemented in our own code, NAP. is about 8× slower than that of the Al-Mg-Si MEAM potential implemented in LAMMPS.

To enable others to reproduce and use the present NN potential, the optimized parameters and a pseudo code to read those parameters are provided in Ref. [28]. The NN potential is implemented also in LAMMPS (it is available on request).

TABLE I. Pure Al bulk properties from experiments or *ab initio* calculations and as computed using the present NN potential and two MEAM potentials (Jelinek and Kim). The structures relevant to these properties are in the training data.

Al	Exp/*ab initio*	NN	Jelinek	Kim
a (Å)	4.05 [31], *4.045*	4.045	4.048	4.047
E_c (eV)	3.39 [32], *3.057*	3.057	3.353	3.360
B (GPa)	72.2 [32], *79.1*	76.9	78.4	79.0
C_{11} (GPa)	114.3 [32], *106.1* [19]	109.9	111.1	113.8
C_{12} (GPa)	61.9 [32], *31.9* [19]	31.6	28.6	31.4
γ_{sf} (mJ/m^2)	135-166 [32,33], *122-164* [29,34–38], *125.8*	116.4	141.9	147.1
γ_{us} (mJ/m^2)	*224* [37,38], *166.2*	156.7	280.9	236.2
$\gamma_{(111)}$ (mJ/m^2)	*710* [38], *720.2*,	742.9	716.1	516.3
$\gamma_{(001)}$ (mJ/m^2)	*873.8*	878.0	1071.6	743.9
$\gamma_{(110)}$ (mJ/m^2)	*927.7*	945.1	1104.8	820.9
α ($10^{-6}/K$)	23.6–25.4 [39]	23.3	14.4	

IV. PROPERTIES OF ALUMINUM

There are a number of interatomic potentials for bulk Aluminum that reproduce most important properties with good accuracy. It is important that the NN potential give similar, or better, properties for the matrix Al material of the Al-Mg-Si alloy. Here, we thus present validation of the NN for pure Al.

Table I shows the bulk properties of FCC Al as obtained by DFT (the reference data), the Jelinek *et al.* MEAM potential (as an example), and the present NN potential. Although the present DFT value of cohesive energy is lower than that of experimental data, the lattice constant, bulk modulus, and other elastic moduli are in good agreement with experimental and previous *ab initio* values. The NN potential reproduces the DFT values of elastic properties with good accuracy.

The generalized stacking fault (GSF) energy is an important property relevant to the dissociation of a perfect dislocation into partial dislocations and to dislocation emission at a crack tip. The GSF energy of a shift vector (x,y) on $\{111\}$ is defined as

$$\gamma^{SF}(x,y) = \frac{E[N](x,y) - N\varepsilon_{Al}}{A}, \tag{8}$$

where N is the number of atoms, A the area of xy plane of the calculation cell, and ε_X the chemical potential of species X, which is the cohesive energy of the most stable structure of the species. Table I shows the stable and unstable stacking fault energies and Fig. 2 shows the GSF curve along the $\langle 112 \rangle$ direction. The NN potential slightly underestimates the *ab initio* results but reproduces the GSF curve well, especially in the range from 0.5 to 1.0 that includes the stable and unstable stacking fault energies.

The dislocation core structure is also important because it is directly related to dislocation motion, dislocation interactions with solutes and precipitates, and is thus at the heart of plasticity mechanisms in metals. Figure 3 shows the Nye tensor distribution around the equilibrated edge dislocation core. The Nye tensor distribution and the partial dislocation separation distance of $3b - 4b$, with $b = 2.86$ Å the Burgers vector, are in very good agreement with full DFT calculations [29,30]. This agreement is generally expected because the

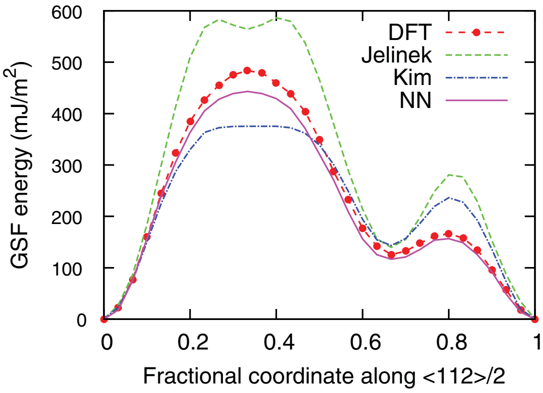

FIG. 2. Generalized stacking fault curve for bulk Al along the [112] direction, as computed using DFT, two MEAM potentials, and the present NN potential. These structures are included in the training data.

NN potential accurately reproduces the controlling stable and unstable stacking fault energies.

The surface energy is defined as

$$\gamma^{\mathrm{surf}}(d) = \frac{E[N](d) - N\varepsilon_{\mathrm{Al}}}{2A}, \tag{9}$$

where d is the separation of two surfaces.

Figure 4 shows the energy versus rigid separation of two blocks of Al as computed by DFT, by two MEAM potentials (Jelinek and Kim), and by the NN potential. The fully-relaxed surface energies $\gamma_{(111)}$, $\gamma_{(001)}$, and $\gamma_{(110)}$ obtained from the largest d are shown in Table I. Although the two MEAM potentials reproduce the order of stability of these surfaces, $\gamma_{(111)} < \gamma_{(001)} < \gamma_{110}$, the Jelinek potential has large unphysical barriers for separation in all the directions and, although they are much smaller, the Kim potential also has unphysical barriers. The NN potential reproduces the DFT curves along all directions and all distances. The NN potential thus accurately reproduces the surface energies but also forces during separation which are the cohesive tractions relevant in fracture processes.

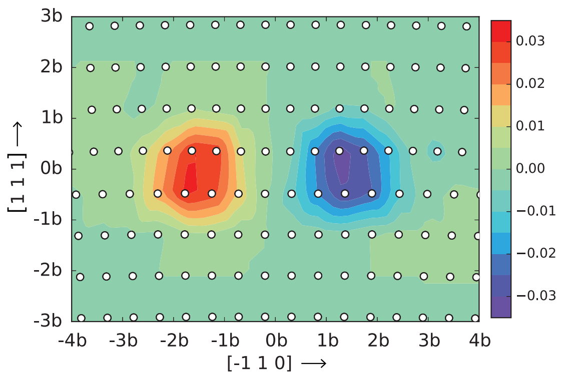

FIG. 3. Nye tensor distribution of the screw component of the Burgers vector for the dissociated edge dislocation core in pure Al; the result agrees well with direct DFT [29,30], x and y axes are in units of the Burgers vector $b = 2.86$ Å. This structure is not in the training data.

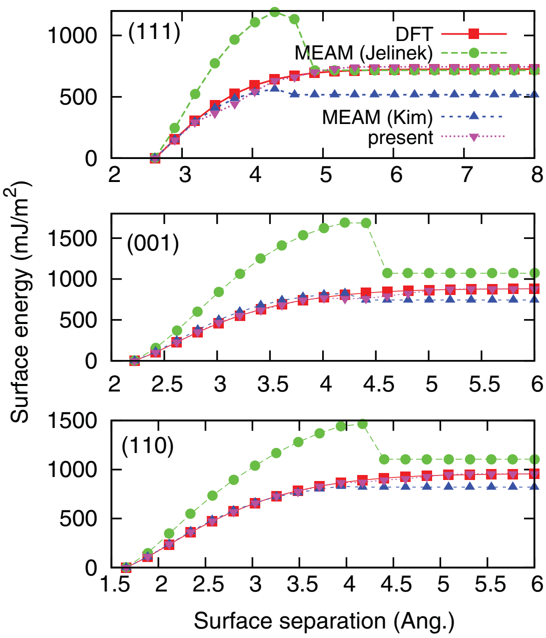

FIG. 4. Energy vs separation for rigid block separation across the (111), (110), and (100) surfaces of bulk Al, as computed via DFT, two MEAM potentials, and the present NN potential. These structures are included in the training data.

We have also performed MD simulation at finite temperatures up to 500 K, which is higher than the normal paint bake temperature of ~450 K used during aging of Al 6xxx alloys, to confirm that the present potential is suitable over the necessary temperature range and also to measure the thermal expansion coefficient. The thermal expansion coefficient is extracted from the slope of the volume-temperature relation as

$$\alpha = \frac{1}{a_0}\left(\frac{da}{dT}\right), \tag{10}$$

where a_0 is the equilibrium lattice constant at 0 K. The α value obtained using the NN potential, shown in Table I, is in good agreement with experimental values. This indicates that the NN potential captures the anharmonicity around the equilibrium lattice constant as well as the harmonic region (related to the bulk modulus).

V. PROPERTIES OF THE TERNARY Al-Mg-Si SYSTEM

We now turn to comparison of the predictions of the NN potential versus DFT for many properties of the Al-Mg-Si ternary system. Note that, although a lot of important structures are included in the training data set, it is impossible to include all the structures of interest because they require large number of atoms or configurations that are not easily calculated by DFT. We will mention in each section, figure and table if the structures are not in the training data.

A. Ordered binary and ternary compounds

The alloy phase with the lowest heat of formation ΔH is the one most likely to form at zero temperature. For accurate modeling of the evolution of the system toward precipitation of the thermodynamically favorable phases, the potential

TABLE II. Lattice constant a (Å) and heat of solutions ΔH^{comp} (meV/atom) for binary and ternary compounds calculated using DFT-PBE, the Jelinek *et al.* MEAM potential, and the present NN potential. *Ab initio* values computed using DFT-PBEsol are indicated in parentheses. These structures are in the training data.

		ab initio		NN		Jelinek	
Composition	Structure	a	ΔH^{comp}	a	ΔH^{comp}	a	ΔH^{comp}
AlMg	B1	*5.745*	*424*	5.760	425	5.714	236
AlMg	B2	*3.388*	*66*	3.396	66	3.440	–31
Al_3Mg	$L1_2$	*4.138*	*4*	4.145	0	4.238	–39
$AlMg_3$	$L1_2$	*4.375*	*5*	4.146	4	4.448	–46
$Al_{12}Mg_{17}$		*10.506*	*–18*	10.539	−18	10.315	389
AlSi	B1	*5.217*	*261*	5.229	261	5.241	280
AlSi	B2	*3.160*	*239*	3.164	239	3.188	142
Al_3Si	$L1_2$	*3.994*	*96*	4.000	96	4.059	113
$AlSi_3$	$L1_2$	*3.899*	*333*	3.907	333	4.194	532
MgSi	B1	*5.505*	*384*	5.532	383	5.507	192
MgSi	B2	*3.308*	*144*	3.313	144	3.384	64
Mg_3Si	$L1_2$	*4.263*	*–7 (−4)*	4.267	−8	4.367	24
$MgSi_3$	$L1_2$	*3.988*	*269*	3.988	269	4.176	322
Mg_2Si	C1	*6.365*	*–136 (−105)*	6.362	−136	6.530	44

must reproduce the heats of formation of many possible alloy phases. The heat of formation of a compound is defined as

$$\Delta H^{\mathrm{comp}} = \frac{E[\{N_{\mathrm{X}}\}] - \sum_{\mathrm{X}} N_{\mathrm{X}} \varepsilon_{\mathrm{X}}}{\sum_{\mathrm{X}} N_{\mathrm{X}}}, \tag{11}$$

where N_{X} is the number of atoms of species X. Table II shows the lattice constants and heats of formation of binary compound phases, Table III shows the equilibrium cell parameters, heats of formation, bulk moduli, and elastic moduli of precipitate phases, as computed by DFT and as

TABLE III. Equilibrium cell parameters, heat of solutions ΔH^{comp} (meV/atom), bulk modulus B (GPa), and elastic constants C_{ij} (GPa) of precipitate structures obtained using the DFT-PBE, the present NN potential and Jelinek *et al.* MEAM potential. The geometry of the preciptate systems follow that employed by Ninive *et al.* [24] (also shown in Fig. 7). Heat of solutions computed using DFT-PBEsol is indicated in parenthese. Elastic constants C_{ij}'s by the *ab initio* caluclation are taken from D. Giofré *et al.* [19]. The structures relevant to these properties are included in the training data.

	Mg_5Si_6			$Al_2Mg_5Si_4$		$Al_3Mg_4Si_4$	
	ab initio	NN	Jelinek	*ab initio*	NN	*ab initio*	NN
a (Å)	*15.138*	15.173	17.012	*15.299*	15.343	*15.095*	15.109
b (Å)	*4.040*	4.074	4.322	*4.044*	4.052	*4.113*	4.131
c (Å)	*6.982*	6.940	7.142	*6.818*	6.846	*6.633*	6.651
α	*90.0*	90.0	89.2	*90.0*	90.0	*90.0*	90.0
β	*110.4*	109.9	89.6	*105.9*	106.0	*106.5*	106.6
γ	*90.0*	90.0	89.9	*90.0*	90.0	*90.0*	90.0
volume ($\mathrm{\AA}^3$)	*400.4*	403.2	525.0	*405.7*	408.9	*395.0*	397.7
ΔH^{comp} (meV/atom)	*18 (24)*	17	311	*–60*	–67	*–32*	–39
B (GPa)	*62.1*	58.5	125.0	*61.2*	62.5	*63.8*	64.4
C_{11} (GPa)	*98.4*	109.4		*107.1*	118.3	*106.7*	110.1
C_{22} (GPa)	*84.6*	94.0		*94.7*	98.6	*96.5*	102.6
C_{33} (GPa)	*88.0*	103.6		*99.1*	112.4	*97.1*	108.5
C_{44} (GPa)	*21.9*	29.8		*26.9*	27.4	*25.9*	30.3
C_{55} (GPa)	*29.1*	38.6		*36.3*	45.3	*35.6*	48.0
C_{66} (GPa)	*51.2*	68.1		*49.4*	60.8	*46.3*	52.7
C_{12} (GPa)	*50.0*	26.1		*40.3*	33.0	*46.5*	36.6
C_{13} (GPa)	*47.7*	46.2		*45.6*	60.0	*48.0*	55.6
C_{23} (GPa)	*45.7*	46.7		*43.0*	44.0	*48.8*	42.3
C_{15} (GPa)	*8.2*	−0.2		*−13.1*	3.6	*9.3*	5.9
C_{25} (GPa)	*5.8*	−2.5		*4.3*	9.5	*5.7*	7.0
C_{35} (GPa)	*5.4*	−1.6		*11.9*	−3.8	*9.3*	−6.2
C_{46} (GPa)	*−10.1*	0.8		*5.4*	2.6	*6.3*	4.8

predicted by the Jelinek *et al.* MEAM potential and the present NN potential. Even for the complex MEAM potential that is calibrated to various binary phases, the prediction of other binary and ternary phases is challenging. In particular, the lattice constants and heats of formation of important Mg-Si phases such as Mg_2Si and Mg_5Si_6 are significantly different from the DFT values. The NN potential, on the other hand, reproduces well the DFT values of the equilibrium cell parameters, bulk moduli, and heats of formation for the important precipitate phases such as Mg_5Si_6, $Al_2Mg_5Si_4$, and $Al_3Mg_4Si_4$ as shown in Table III. Tables II and III include some *ab initio* values of heat of formation obtained using the PBEsol functional, from which we see that the difference between DFT with PBE and NN potential is smaller than the difference between DFT with PBE and PBEsol, i.e., the NN potential is within the accuracy of the DFT itself. The difference in lattice constants for Mg_5Si_6 and FCC Al for the NN potential is less than 1%, indicating that the precipitates of Mg_5Si_6 in Al matrix will be stable and remain coherent when using the NN potential. Some of the shear elastic constants of NN potential differ from those of DFT and could contribute the difference in formation energies of precipitates in Al matrix, which are evaluated in Sec. V D.

B. Single solute and vacancy properties

Heats of solution of isolated solutes in FCC Al are important because they are relevant to the solid solution phase and thus to the stability of ordered phases relative to the solid solution state. The heat of formation of a vacancy is related to equilibrium and nonequilibrium vacancy concentrations and thus to vacancy-mediated diffusion of solutes and matrix atoms. The heat of solute or formation energy is computed as

$$\Delta H^{\mathrm{sol}} = E[\mathrm{Al}_{(N-1)}\mathrm{X}_1] - (N-1)\varepsilon_{\mathrm{Al}} - \varepsilon_{\mathrm{X}}, \qquad (12)$$

where X denotes the solute or vacancy, and we hereafter treat a vacancy as a "solute" with $\varepsilon_{\mathrm{Vac}} = 0$.

Table IV shows the calculated heats of solution via DFT, the two MEAM potentials, and the present NN potential. The Kim MEAM potential gives quite good values for the heats of formation for Mg and vacancy, whereas the Jelinek MEAM potential is not good for these solutes. This shows the difficulty in constructing MEAM potentials for more than two elements. The NN potential predictions for the heats of solution for Mg and Si agree well with those computed by DFT.

Table IV also shows the misfit volumes of Mg and Si calculated by DFT and the NN potential. The DFT misfit volumes are taken from Leyson *et al.* [30] and the NN potential misfit volumes are calculated using the same method. The NN potential underestimates the misfit volume of Mg by about 10%. This is acceptable for reasonable estimates of the interaction energy of Mg with the Al dislocation or with precipitate-induced pressure fields. The misfit volume of Si is in very good agreement with the DFT result.

TABLE IV. Heats of formation ΔH^{sol} (eV) and misfit volumes ($\mathrm{\AA}^3$) (in parentheses) of a substitutional solute and vacancy in FCC Al. These values are obtained from 4 × 4 × 4 cubic FCC cells that are not in the training data, but the relevant structures with 2 × 2 × 2 cubic FCC cells are included in the training data.

Substitute	*ab initio*	NN	Jelinek	Kim
Mg	*0.090 (5.71)*	0.100 (5.15)	−0.200	0.098
Si	*0.375 (−2.65)*	0.376 (−2.63)	0.500	
Vacancy	*0.654*	0.647 (−3.39)	0.670	0.708

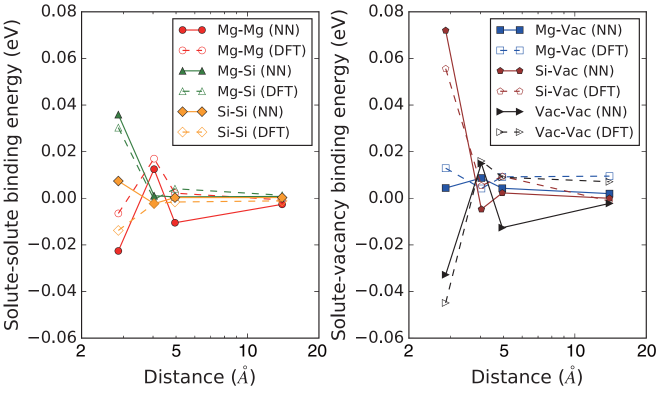

FIG. 5. (a) Solute-solute binding energies as a function of distance between solutes, and (b) solute-vacancy binding energies, obtained by the NN potential (filled markers and solid lines) and DFT (open markers and broken lines). These values are obtained using 4 × 4 × 4 cubic FCC cells which are not in the training data, but the relevant structures with 2 × 2 × 2 cells are in the training data.

C. Solute-solute binding and energies of solute clusters

The interactions among solutes and vacancies is crucial to the early stage formation of solute clusters during aging. Trapping of vacancies by clusters (so-called "vacancy prisons" [40]) has been suggested as important in Al-6xxx aging in particular. A useful potential must therefore reproduce these binding energies within approximately an energy of k_BT to provide accurate metastable energetics during the evolution of the system.

The binding energy between two solutes X and Y is defined as

$$-E_{\mathrm{bind}}^{\mathrm{X-Y}} = E[\mathrm{Al}_{(N-2)}\mathrm{X}_1\mathrm{Y}_1] + N\varepsilon_{\mathrm{Al}} - E[\mathrm{Al}_{(N-1)}\mathrm{X}_1] - E[\mathrm{Al}_{(N-1)}\mathrm{Y}_1]. \qquad (13)$$

With this definition, a positive value indicates that X and Y tend to bind to each other. Figure 5(a) shows the binding energies of pairs among Mg and Si versus pair separation distance, and Fig. 5(b) the binding energies that involve a vacancy, as computed by the DFT and as predicted by the NN potential. These values are obtained using 4 × 4 × 4 cubic FCC cells and these structures are not in the training data, but the relevant structures with 2 × 2 × 2 cells are in the training data. The figures show that the differences between the NN prediction and the DFT computation are less than 20 meV in all cases, which is slightly below $k_BT = 25.4$ meV at $T = 293$ K. The sign of the nearest-neighbor binding of Si-Si is the opposite of the DFT results, but the absolute value is small so that this difference is not of great consequence at the temperatures of interest. Of more importance are the trends of strong binding between Si-Vac and Mg-Si, and the repulsive interaction between vacancies, all of which are predicted well

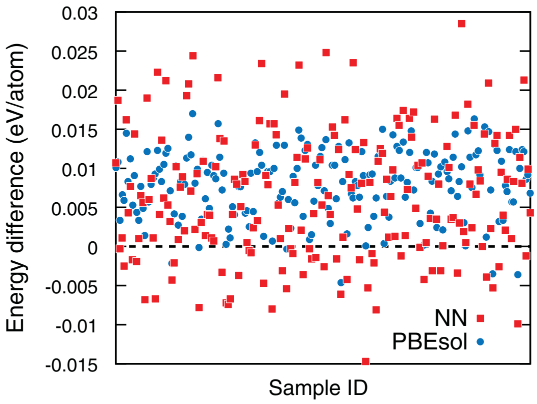

FIG. 6. Formation energies per atom of the system described in Sec. II obtained by the NN potential (red squares) and the DFT-PBEsol (blue circles), as differences from the DFT-PBE results. Since these structures are not in the training data set, this can be treated as the prediction error of solution/precipitation energies by the NN potential.

with the NN potential. These results indicates that the NN potential can be useful for meaningful simulations of clustering of solutes.

An important observation we made is that the interaction energy between solutes depend strongly on the size of the supercell, more than would be expected based on misfit volume and elastic terms. We traced the source of this discrepancy to long-range charge oscillations induced by the solute atom. These kinds of long-range effects cannot be captured by a short-range NN potenial, which partially explains the difficulty in accurately learning solute interaction energies. We note, however, that the accuracy we can achieve is sufficient for the modeling of the early stages of precipitation in Al6xxx alloys: treatment of long-range effect will be the subject of further studies.

To move beyond simple pair interactions toward larger clusters such as those that might emerge during aging, we have also computed the heats of formation of rather complex random Al-Mg-Si-vacancy configurations via both DFT and the NN potential. The many specific configurations studied here (consisting of 16 Al atoms, 2 vacancies, and a total of 14 Mg and Si atoms) are not important on their own, and hence we do not show all the structures but rather concentrate on the spectrum of energies. Figure 6 shows the difference in formation energies of all configurations as computed by the NN potential and by DFT. The formation energy is defined as

$$E_f = E[N_{\mathrm{Al}},N_{\mathrm{Mg}},N_{\mathrm{Si}}] - N_{\mathrm{Al}}\varepsilon_{\mathrm{Al}} - N_{\mathrm{Mg}}\varepsilon_{\mathrm{Mg}}^{\mathrm{SS}} - N_{\mathrm{Si}}\varepsilon_{\mathrm{Si}}^{\mathrm{SS}}, \quad (14)$$

where $\varepsilon_{\mathrm{X}}^{\mathrm{SS}} \equiv E[\mathrm{Al}_{255}\mathrm{X}_1] - 255\varepsilon_{\mathrm{Al}}$ is the solid solution energy of solute X. Since these configurations are not included in the training data set, these results provide a measure of transferability, or conversely error prediction, for the present NN potential for solute clusters. The mean difference is +6 meV/atom with a standard deviation of +/−8 meV/atom. Figure 6 also shows the differences between PBE and PBEsol DFT results, with a mean difference of +8 meV/atom and standard deviation of +/−4 meV/atom. The NN potential predictions are thus somewhat larger than the differences among different DFT methods, but are almost within the statistical scatter. In contrast, the Jelinek MEAM potential predicts differences with DFT of mean +256 meV/atom and standard deviation +/−108 meV/atom, which are not only 10–20 times larger, but far too large to be suitable for studies of aging.

D. Precipitates

In the early stages of precipitation in Al-Mg-Si alloys, the Mg/Si ratio in a needle-shape precipitate is smaller than that of the larger equilibrium $\mathrm{Mg_2Si}$ precipitate, which has the C1 structure. The structure of the early-stage precipitate is thought to be $\mathrm{Mg_5Si_6}$ [41] or the same crystalline structure but with some Mg or Si atoms replaced by Al [24] as shown

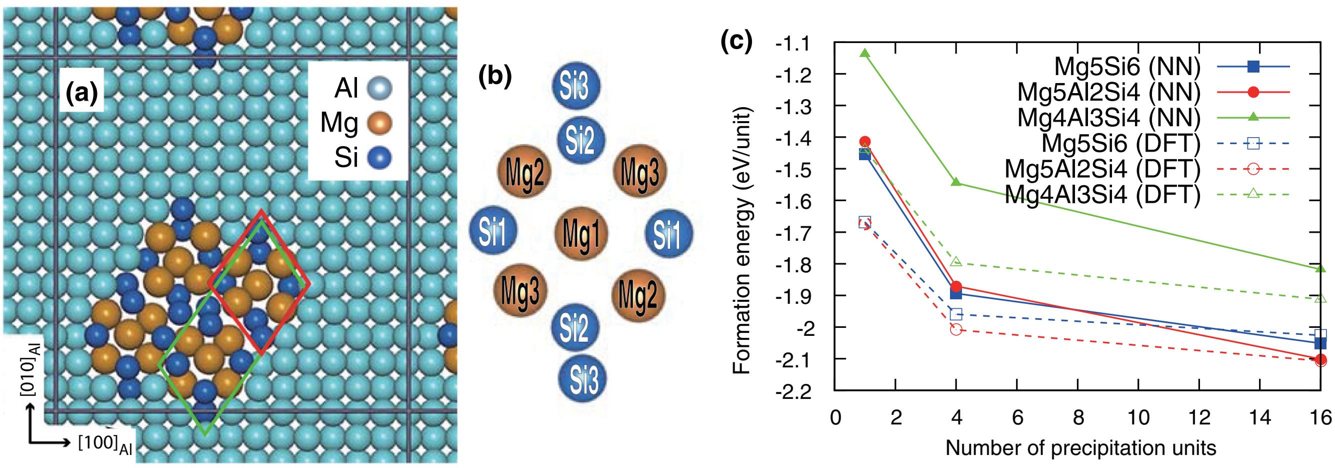

FIG. 7. (a) Typical simulation cell of $\mathrm{Mg_5Si_6}$ precipitate of $N_{\mathrm{FU}} = 4$ in Al matrix, which corresponds to 7 × 7 × 1 FCC Al cell. The system is periodic in z direction, $[001]_{\mathrm{Al}}$. The green rectangle indicates a monoclinic cell of $\mathrm{Mg_5Si_6}$. (b) Formation unit of $\mathrm{Mg_5Si_6}$ indicated in the red rectangle in (a). In case of $\mathrm{Mg_5Al_2Si_4}$, $\mathrm{Si_3}$ sites in $\mathrm{Mg_5Si_6}$ are replaced by Al, while $\mathrm{Mg_1}$ site is also replaced by Al in $\mathrm{Mg_4Al_4Si_4}$. (c) Size dependency of the precipitation energy of $\mathrm{Mg_5Si_6}$, $\mathrm{Al_2Mg_5Si_4}$, and $\mathrm{Al_3Mg_4Si_4}$ obtained by the NN potential and the DFT (from D. Giofré *et al.* [19]). These structures are not in the training data set.

in Fig. 7(a). We have thus computed the formation energies of these precipitates as a function of size when embedded in the Al matrix using the NN potential and have compared the predictions with DFT results. The DFT study is similar in spirit to that of Ninive *et al.*, but not identical in terms of implementation and boundary conditions [19]. The simulation cells here for both DFT and NN are identical, making direct comparison possible. These structures are not in the training data set and thus the comparison shows prediction errors of the NN potential for precipitates.

The precipitate energy is defined as

$$E_{\mathrm{prec}} = E_{\mathrm{f}}/N_{\mathrm{FU}}, \tag{15}$$

where E_{f} is defined in Eq. (14) and N_{FU} the number of precipitate formula units in the precipitate, as shown in Fig. 7(a). Figure 7(c) shows the precipitate energies obtained by DFT and by the NN potential as a function of N_{FU}. The DFT and NN results are in good agreement for larger precipitates, but the NN potential underestimates the precipitate stability for the smallest precipitates (one formula unit), with a difference of ∼0.2–0.3 eV/unit. These energy differences are thus rather larger than those found for individual solute-solute interactions on a per-atom basis as the one precipitate unit contains 11 atoms. If we assume that not only precipitate atoms but also surrounding Al atoms, for example, Al atoms interacting with the precipitate within the cutoff range of the NN potential, are contributing to the energy difference, it would decrease close to the uncertainty of the DFT method found for the 32-atom Al-Mg-Si-vacancy clusters.

Proceeding further, the contributions to the precipitation energy can be divided into four parts: the bulk formation energy, the strain energy, and contributions from interfaces and edges. The E_{prec}, which is the precipitation energy per N_{FU}, of bulk and strain parts are independent of N_{FU}, while the interface and edge energies should scale as $N_{\mathrm{FU}}^{-1/2}$ and N_{FU}^{-1}, respectively. Therefore, as N_{FU} increases, the bulk and strain energies should dominate E_{prec} while the edge contribution could be significant at small sizes, e.g., $N_{\mathrm{FU}} = 1$. The good accuracy of the bulk formation energy and elastic constants as shown in Tables I and III the underestimation of the NN potential for the small precipitates with $N_{\mathrm{FU}} = 1$ implies that the NN potential overestimates the formation energies of the precipitate edges and surfaces. Of course, one precipitate unit (11 atoms) is nearly entirely "interface" and "edges," and hence deviations per atom are comparable to the deviations for other solute-solute interaction energies. Nonetheless, the cumulative effect of these per-atom energy differences (reaching 0.2–0.3 eV/unit) can have an effect on overall aging behavior since the total difference in precipitate energy is not negligible. Improving the error of these energy differences is still challenging even for the machine-learning potential like NN and may not be necessary because the uncertainty of the DFT method could also result in non-negligible differences.

E. Dislocation-solute interaction

Interactions between solute and dislocation core, and solute and stacking fault between dissociated dislocations are important properties for the solution strengthening and for modeling dislocation motion in alloys. The interaction energy is computed as

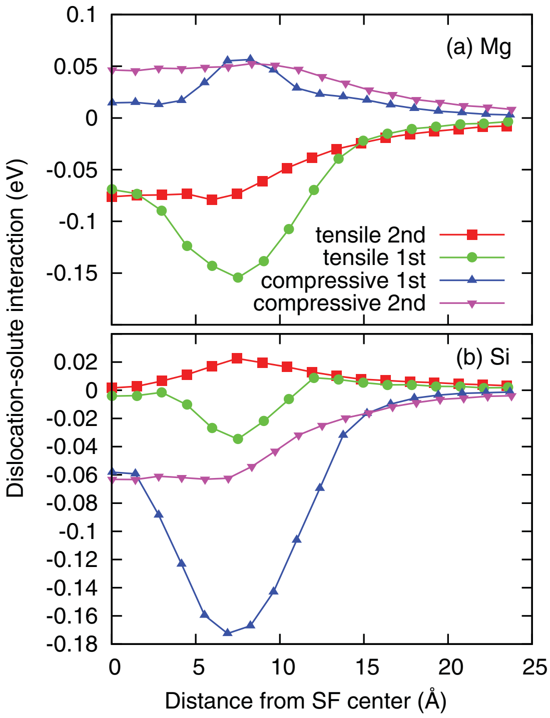

FIG. 8. Interactions between a dissociated dislocation core in Al and a solute in (a) Mg and (b) Si. These structures are not in the training data set.

$$E_{\mathrm{int}}^{\mathrm{disl-sol}}(x_i,y_j) = E^{\mathrm{disl-sol}}(x_i,y_j) - [E^{\mathrm{disl}} + E^{\mathrm{sol}}], \tag{16}$$

where $E^{\mathrm{disl-sol}}(x_i,y_j)$ is the total energy of the system including the dislocation and the solute atom at position (x_i,y_j) from the center of the stacking fault, and E^{disl} is the total energy of the system including the dislocation without solute. E^{sol} is the solid solution energy defined as

$$E^{\mathrm{sol}} = \frac{1}{N_{\mathrm{layer}}} \sum_{j}^{N_{\mathrm{layer}}} [E^{\mathrm{disl-sol}}(x_{\mathrm{far},j},y_j) - E^{\mathrm{disl}}], \tag{17}$$

where N_{layer} is the number of layers considered, which is four in this study, and $x_{\mathrm{far},j}$ is the x position farthest from the center of stacking fault within the jth layer. Since modeling solute-dislocation interaction requires large system with more than 10 000 atoms, these structures are not in the training data and thus these properties also show prediction errors of the NN potential.

Figure 8 shows the interactions between a dislocation centered at the origin and a single solute at different (x_i,y_j) positions. Since the misfit volume of Mg in Al is positive, Mg has negative interaction energy at positions lying on that side of the dislocation glide plane where the local pressure field is tensile, and a positive interaction energy at positions on the compressive side. The range of the interaction energy is about 0.2 eV, which is in good agreement with DFT [30]. Conversely, since the Si misfit volume in Al is negative, the interaction energy between the dislocation and Si atoms should be negative (binding) on the compressive side of the glide plane and positive on the tensile side. However, Fig. 8(b) shows that the interaction energy for Si atoms close to the partial dislocation core tends to become negative even if Si is on the tensile side; this is not seen in the DFT calculations [30]. In addition, on the compressive side near the partial cores, the interaction energy is somewhat larger (2×–3×) than the DFT values. Since the misfit volume of Si in Al is captured well by the NN potential (Table IV), the NN potential prediction of strong binding of Si in the partial dislocation core stems from an artificial "chemical" interaction in this region of high lattice distortion core. The NN potential is thus inaccurate for this situation, which will influence predictions of the solute-strengthening of dislocations as they move through a field of Si solutes. This may also impact dislocation interactions with Si-containing precipitates, for which there are no reference DFT computations.

VI. CONCLUSION

We have developed an NN potential for studying the precipitation strengthening in the ternary Al-Mg-Si alloy. The NN potential is trained to reproduce DFT energies and forces for numbers of structures including several bulk phases, surfaces, stacking faults, vacancies, and solid solutions. The NN potential is accurate in its prediction of (i) the lattice constant, bulk modulus, elastic moduli, stacking-fault, and surface energies of pure Al, (ii) the solute/solute and solute/vacancy binding energies to within 20 meV/pair, relative to the DFT results. Errors for properties included in the training data set are smaller than the uncertainties in the DFT method, as assessed by comparisons of DFT using two exchange-correlation functionals for a subset of properties. Errors for properties not included in the training data set are slightly larger but still generally comparable to the uncertainty of the DFT method.

Only the Si/dislocation interaction energies near the partial cores of the Al edge dislocation show differences that could be important for quantitative predictions of strengthening. The energies of small Al-Mg-Si clusters are also less accurate than other quantities, although not significantly on a per-atom basis, but trends with size and composition are followed quite well. Since the machine-learning-type potentials such as the NN potential are basically interpolating a potential energy landscape, these inaccurate properties could be improved by including training data such as dislocation core structures and small precipitate structures unless they have intrinsic long-range interactions that cannot be captured by the short-range NN potential as we observed for solute-solute interactions. We also note that certain DFT results (dislocation structure [29,30], dislocation/solute interactions and solute misfits [30]) were calculated using different codes and possibly different specific parameters such as the *k*-point mesh and the cutoff energy, and the dislocation cases using a multiscale method—therefore, in all of these cases, some differences are expected within the error/uncertainty of these other DFT numbers. These differ from the DFT results used in the training data.

The overall success of the NN potential indicates that it can be used for the studies of precipitate strengthening of Al-Mg-Si alloys involving the evolution of solute clusters, early formation of nanoprecipitates, and their interactions with dislocations. More broadly, these results show that machine-learning-type potentials such based on the neural networks can be quantitatively successful, and thus powerful tools, for modeling complex alloys that have proven to be extremely challenging cases for the other physics-based interatomic potential formulations.

ACKNOWLEDGMENTS

This work was supported in part by "Materials research by Information Integration" Initiative (MI^{2}I) project of the Support Program for Starting Up Innovation Hub from Japan Science and Technology Agency (JST). W.A.C. acknowledges support of this work through a European Research Council Advanced Grant, "Predictive Computational Metallurgy," ERC grant agreement No. 339081 PreCoMet. D.G. and M.C. acknowledge support for this work by an Industrial Research Grant funded by Constellium.

---

[1] M. S. Daw and M. I. Baskes, Phys. Rev. B **29**, 6443 (1984).
[2] B. J. Lee and M. I. Baskes, Phys. Rev. B **62**, 8564 (2000).
[3] B. Jelinek, J. Houze, S. Kim, M. F. Horstemeyer, M. I. Baskes, and S.-G. Kim, Phys. Rev. B **75**, 054106 (2007).
[4] B.-J. Lee, W.-S. Ko, H.-K. Kim, and E.-H. Kim, Calphad **34**, 510 (2010).
[5] J. Behler and M. Parrinello, Phys. Rev. Lett. **98**, 146401 (2007).
[6] A. P. Bartók, M. C. Payne, R. Kondor, and G. Csányi, Phys. Rev. Lett. **104**, 136403 (2010).
[7] A. P. Bartók and G. Csányi, Int. J. Quantum Chem. **115**, 1051 (2015).
[8] A. Seko, A. Takahashi, and I. Tanaka, Phys. Rev. B **90**, 024101 (2014).
[9] N. Artrith, B. Hiller, and J. Behler, Phys. Status Solidi (b) **250**, 1191 (2012).
[10] N. Artrith and A. Urban, Comput. Mater. Sci. **114**, 135 (2016).
[11] G. C. Sosso, G. Miceli, S. Caravati, J. Behler, and M. Bernasconi, Phys. Rev. B **85**, 174103 (2012).
[12] S. Hajinazar, J. Shao, and A. N. Kolmogorov, Phys. Rev. B **95**, 014114 (2017).
[13] C. Cavazzoni, M. Cococcioni, I. Dabo, G. Sclauzero, R. Car, S. Fabris, A. Smogunov, C. Gougoussis, P. Giannozzi, A. P. Seitsonen *et al.*, J. Phys.: Condens. Matter **21**, 395502 (2009).
[14] J. P. Perdew, K. Burke, and M. Ernzerhof, Phys. Rev. Lett. **77**, 3865 (1996).
[15] D. Vanderbilt, Phys. Rev. B **41**, 7892 (1990).
[16] Standard Solid State Pseudopotentials (SSSP), http://materialscloud.org/sssp/.
[17] J. P. Perdew, A. Ruzsinszky, G. I. Csonka, O. A. Vydrov, G. E. Scuseria, L. A. Constantin, X. Zhou, and K. Burke, Phys. Rev. Lett. **100**, 136406 (2008).
[18] NAP (Nagoya Atomistic-simulation Package), https://github.com/ryokbys/nap.

[19] D. Giofré, T. Junge, W. A. Curtin, and M. Ceriotti (unpublished).
[20] Y. M. Kim, N. J. Kim, and B. J. Lee, Calphad **33**, 650 (2009).
[21] S. Plimpton, J. Comput. Phys. **117**, 1 (1995).
[22] R. Biswas and D. R. Hamann, Phys. Rev. B **34**, 895 (1986).
[23] H. J. C. Berendsen, J. P. M. Postma, W. F. van Gunsteren, A. DiNola, and J. R. Haak, J. Chem. Phys. **81**, 3684 (1984).
[24] P. H. Ninive, A. Strandlie, S. Gulbrandsen-Dahl, W. Lefebvre, C. D. Marioara, S. J. Andersen, J. Friis, R. Holmestad, and O. M. Løvvik, Acta Mater. **69**, 126 (2014).
[25] C. S. Hartley and Y. Mishin, Acta Mater. **53**, 1313 (2005).
[26] G. Montavon, G. Orr, and K.-R. Müller, *Neural Networks: Tricks of the Trade*, Lecture Notes in Computer Science Vol. 7700 (Springer, Berlin, Heidelberg, 2012).
[27] W. H. Press, S. A. Teukolsky, W. T. Vetterling, and B. P. Flannery, *Numerical Recipes in Fortran 90*, *The Art of Parallel Scientific Computing* (Cambridge University Press, Cambridge, 1996).
[28] See Supplemental Material at http://link.aps.org/supplemental/10.1103/PhysRevMaterials.1.053604 for the list of NN potential parameters and the detailed description about a pseudo code that reads these parameters for the use of NN potential program.
[29] C. Woodward, D. R. Trinkle, L. G. Hector, and D. L. Olmsted, Phys. Rev. Lett. **100**, 045507 (2008).
[30] G. P. M. Leyson, L. G. Hector Jr., and W. A. Curtin, Acta Mater. **60**, 3873 (2012).
[31] N. W. Ashcroft and N. D. Mermin, *Solid State Physics* (Saunders College Publishing, Philadelphia, 1976).
[32] C. Kittel, *Introduction to Solid State Physics*, 8th ed. (Wiley, Hoboken, NJ, 2005).
[33] R. E. Smallman and P. S. Dobson, Metall. Trans. **1**, 2383 (1970).
[34] S. Crampin, K. Hampel, D. D. Vvedensky, and J. M. MacLaren, J. Mater. Res. **5**, 2107 (1990).
[35] P. J. H. Denteneer and J. M. Soler, J. Phys.: Condens. Matter **3**, 8777 (1991).
[36] B. Hammer, K. W. Jacobsen, V. Milman, and M. C. Payne, J. Phys.: Condens. Matter **4**, 10453 (1992).
[37] G. Lu, N. Kioussis, V. V. Bulatov, and E. Kaxiras, Phys. Rev. B **62**, 3099 (2000).
[38] X.-Z. Wu, R. Wang, S.-F. Wang, and Q.-Y. Wei, Appl. Surf. Sci. **256**, 6345 (2010).
[39] A. J. C. Wilson, Proc. Phys. Soc. **53**, 658 (1941).
[40] S. Pogatscher, H. Antrekowitsch, H. Leitner, T. Ebner, and P. J. Uggowitzer, Acta Mater. **59**, 3352 (2011).
[41] H. W. Zandbergen, S. J. Andersen, and J. Jansen, Science **277**, 1221 (1997).